# Band alignment and electronic structure of the anatase TiO_{2}/SrTiO_{3}(001) heterostructure integrated on Si(001)

Hosung Seo, Agham B. Posadas, Chandrima Mitra, Alexander V. Kvit, Jamal Ramdani, and Alexander A. Demkov

Phys. Rev. B **86**, 075301 — Published 1 August 2012

DOI: 10.1103/PhysRevB.86.075301

**Band alignment and electronic structure of the anatase $TiO_2/SrTiO_3$ (001) heterostructure integrated on Si(001)**

Hosung Seo[a], Agham B. Posadas[a], Chandrima Mitra[a], Alexander V. Kvit[b], Jamal Ramdani[c], and Alexander A. Demkov[a1]

[a]Department of Physics, The University of Texas at Austin, Austin, Texas 78712, USA

[b]Department of Materials Science and Engineering, University of Wisconsin at Madison, Madison, WI 53706, USA

[c]National Semiconductor, Santa Clara, CA 95052, USA

**Abstract**

Using density functional theory (DFT), scanning transmission electron microscopy (STEM), and electron energy loss spectroscopy (EELS) we study the interface structure and electronic properties of the anatase-$TiO_2/SrTiO_3$(001) heterostructure epitaxially grown on Si (001) by molecular beam epitaxy (MBE). We show that charge transfer at the $TiO_2/SrTiO_3$ interface is induced by the chemical bond formation between Ti and O. Subsequent O lattice polarization is found to be the leading screening mechanism at the interface. By comparing the theoretical local electronic structure to the O *K* edge EELS spectra taken at the interface with atomic resolution, we are able to trace how the local band structure evolves in response to the change in symmetry and bonding across the interface. We also discuss the effect of interfacial point defects (O vacancy and F impurity) on the band alignment.

## I. Introduction

Anatase $TiO_2$ is the subject of extensive research efforts owing to its energy and environmental applications [1-4]. The conduction band edge of $TiO_2$ is well matched to the redox potential of water, making it an excellent candidate for hydrogen production via photocatalytic water splitting [5]. This material system is promising due to its relatively high efficiency, chemical stability in water, non-toxicity, and low production cost [1]. Among the three polymorphs of $TiO_2$ (rutile, anatase, and brookite), the most abundant phase in nature is rutile (space group $P4_2/mnm$). However, it has been found that anatase (space group $I4_1/amd$) shows significantly higher photocatalytic activity than rutile [5]. This has been attributed to the higher reactivity of the anatase (001) surface [6,7], higher mobility of the charge carriers [8,9], and longer electron-hole pair lifetime [10].

The main challenge for photocatalytic applications is the rather large band gap of anatase $TiO_2$ (approximately 3.2 eV making it ultraviolet-active) and high recombination rate of the photo-excited electron-hole pairs [11]. A variety of methods for band gap engineering have been proposed to utilize solar-abundant visible light instead of ultraviolet, including nitrogen-doping [12], co-doping [13,14], and surface hydrogenation [15]. In order to overcome these challenges, oxide interface engineering has attracted considerable attention [16-19]. In addition to band gap engineering at the interface, a longer lifetime of photo-excited electron-hole pairs could be achieved, for example, by spatially separating the carriers across the interface using a staggered band alignment. However, a clear understanding of the interface effects on the photocatalytic activity of mixed oxide catalysts is lacking, in particular due to a limited number of model systems where such a connection can be traced [20].

[1] demkov@physics.utexas.edu

Since the thermodynamically stable bulk phase of $TiO_2$ at room temperature and ambient pressure is rutile, single crystal anatase is typically synthesized only in the form of nanoparticles [2,6]. However, recent advances in oxide heteroepitaxy, have made it possible to grow high-quality, single crystal anatase films on perovskite substrates such as $SrTiO_3$ (STO) or $LaAlO_3$ (LAO) [21,22]. This provides an excellent model system for controlled studies of the photocatalytic behavior of anatase under various conditions [23-25]. Burbure *et al.* have shown that for anatase-$TiO_2$/$BaTiO_3$ structures, dipole fields from the underlying ferroelectric domains separate holes and electrons, leading to spatially selective photochemical reactions at the anatase surface [23]. Kazazis and co-workers have reported that the photocatalytic activity at the surface of anatase deposited on Si (111) can be controlled by changing the Fermi level position of the Si substrate [24]. Moreover, a number of interesting physical phenomena and potential applications of anatase/perovskite oxide heterostructures have been reported, including thermoelectric and spintronic applications [26-30].

While a considerable amount of experimental work can be found in the literature, a detailed theoretical understanding of the electronic structure of the anatase-$TiO_2$/perovskite interface is lacking. Such knowledge could suggest new ways of manipulating the band structure and band alignment, which are crucial in high efficiency hydrogen production using sunlight, making this system of significant fundamental and practical interest. Recently, Chambers *et al.*, using x-ray photoelectron spectroscopy (XPS), have reported that there is no measurable valence band offset between anatase $TiO_2$ (001) and STO (001) [31]. Curiously, in contradiction with the XPS result, their DFT calculations suggest a valence band offset of 0.5 eV. This could be interpreted either as the inability of DFT to fully account for the interface properties or that the atomic structure used in the calculation differs from the experimental one. We feel that in view of its importance, the band alignment problem at this interface warrants revisiting.

In this paper, we consider a heterojunction of anatase with STO grown on Si. Using MBE, we grow epitaxial *c*-axis oriented anatase on an STO/Si (001) pseudo-substrate [32], and use Z-contrast STEM to elucidate the real physical structure of the interface. EELS is used to probe the electronic structure across the interface. The interface geometry inferred from STEM is used in DFT calculations, which are then validated by comparing the theoretical density of states with the O *K* edge EELS structure. The paper is organized as follows: first, we briefly introduce the computational methodology used in the paper and describe the anatase MBE growth. This is then followed by a detailed analysis of the electronic structure of the interface including charge transfer, dielectric screening and the possible role of point defects.

## II. Methodology

*1. Theory*

We use DFT as implemented in the VASP code [33]. The exchange-correlation energy is treated within the local density approximation (LDA), using the Ceperley-Alder data parameterized by Perdew and Zunger [34]. We employ projector augmented wave pseudopotentials to describe Sr, Ti, and O [35]. Valence electron configurations for the elements are $4s^2 4p^6 5s^2$ for Sr, $3d^2 4s^2$ for Ti, and $2s^2 2p^4$ for O. We use a cutoff energy of 600 eV for the plane wave expansion. The electronic total energy is converged to $10^{-6}$ eV/cell. We fully relax the internal ionic degrees of freedom until the Hellmann-Feynman forces are less than 10 meV/Å. We employ 6×6×6 and 6×6×4 Monkhorst-type *k*-point meshes to integrate over the

Brillouin zone for cubic STO and tetragonal anatase $TiO_2$, respectively. We calculate the STO lattice parameter $a$ to be 3.873 Å, and the $TiO_2$ lattice parameters $a$ and $c$ to be 3.766 Å and 9.456 Å ($c/a$=2.511), respectively. These are in good agreement with low temperature experimental values of $a$ = 3.897 Å for STO [36], and $a$ = 3.780 Å and $c$ = 9.491 Å ($c/a$=2.511) for anatase $TiO_2$ [37] that are extrapolated based on the thermal expansion coefficients. Thus, theoretical biaxial tensile strain in the anatase film on STO (001) is calculated to be 2.8%, which agrees well with the experimental value of 3.0%.

To model the evolution of the valence band with the anatase film thickness, we use several supercells. We model the substrate with a five unit cell thick $TiO_2$-terminated STO (001) slab. We consider 4, 6, and 8 monolayers (MLs) of anatase (one anatase unit cell has four MLs) on both sides of STO to take into account any interface and surface dipoles within the periodic boundary conditions. The supercell with 8 MLs of anatase is shown in Fig. 1. The slab in each computational cell is separated from its nearest neighbor images in the $c$-direction by 14 Å of vacuum to avoid spurious slab-slab interactions. We consider two types of supercells in terms of the in-plane cell size. To study the basic properties of the interface, we use a 1×1 in-plane cell. We increase the cell size to $\sqrt{2}\times\sqrt{2}$ to calculate the O $K$-edge spectra, O vacancy, and F impurity at the interface. We use a 6×6×2 $k$-point mesh for the 1×1 supercells. For the $\sqrt{2}\times\sqrt{2}$ calculations, a 4×4×2 $k$-point grid is used for the structural relaxation while a 6×6×2 grid is used for the total energy and density of states calculations.

To investigate whether the LDA causes the incorrect band offset prediction as suggested in Ref. [31], we use a quasi-particle (QP) correction within the $G_oW_o$ approximation as implemented in the VASP code [38]. In principle, the QP energies are obtained by solving the equation:

$$(T+V_{ext}+V_H)\psi_{nk}(\mathbf{r})+\int \mathbf{dr'}\Sigma(\mathbf{r},\mathbf{r'}:E_{nk})\psi_{nk}(\mathbf{r'})=E_{nk}\psi_{nk}(\mathbf{r}), \qquad (1)$$

where $T$ is the kinetic energy of the electrons, $V_{ext}$ is the external potential of the ions, and $V_H$ is the Hartree potential. The energy dependent non-local self-energy operator $\Sigma$ contains the exchange and correlation effects, and within Hedin's $GW$ approximation [39], it takes the form:

$$\Sigma(\mathbf{r},\mathbf{r}':\omega)=\frac{i}{4\pi}\int_{-\infty}^{\infty} e^{i\omega'\delta}G(\mathbf{r},\mathbf{r}',\omega+\omega')W(\mathbf{r},\mathbf{r}',\omega')d\omega', \qquad (2)$$

where $G$ is the Green's function and $W$ is the screened Coulomb interaction. Then to first order the QP eigenvalues of equation (1) are obtained as:

$$E_{nk}^{QP}=\langle\psi_{nk}|T+V_{ext}+V_H+\Sigma|\psi_{nk}\rangle \qquad (3)$$

In a non-self-consistent $G_0W_0$ approximation, which has been shown to be a quite reasonable approximation [39,40], the $\psi_{nk}$ are chosen to be the Kohn-Sham LDA wave functions. For our calculations we choose a plane-wave cutoff of 680 eV for both STO and $TiO_2$. The number of bands used is 300 and 620 for STO and $TiO_2$, respectively. For the frequency integration in equation (2) we use 50 frequency grid points. The QP eigenvalues are converged to 0.03 eV.

*2. Experiment*

Anatase is deposited using MBE on a $SrTiO_3$ layer that has been epitaxially grown on Si (001). The Si wafer is first degreased and exposed to ultraviolet/ozone prior to loading into the growth chamber. After desorption of the native $SiO_2$ using a Sr-assisted deoxidation process [41], 50 Å of crystalline $SrTiO_3$ with $TiO_2$ termination is deposited on Si with the aid of a ½ monolayer Sr template [32,42] at a substrate temperature of 550°C and a background oxygen pressure of $4\times10^{-7}$ torr. The substrate temperature is then quickly increased to 650°C, while oxygen pressure is slowly ramped to $1\times10^{-6}$ torr for the anatase $TiO_2$ deposition. Samples with total thicknesses of 10-40 monolayers of anatase (one anatase unit cell equals four MLs) are deposited on $SrTiO_3$/Si. The growth of all the layers is monitored *in situ* using reflection high energy electron diffraction (RHEED). Typical RHEED patterns for both $SrTiO_3$ and anatase are shown in Fig. 2. Fig. 2 (a) shows a RHEED pattern taken along the Si<110> ($SrTiO_3$<100>) direction for a 5 nm $SrTiO_3$ film grown on Si(001). Fig. 2 (b) shows a RHEED pattern for a 20 monolayer anatase film taken along the same direction. The anatase surface shows a 4×1 surface reconstruction typically exhibited by well-ordered epitaxial anatase films [21].

After growth, the samples are prepared for cross-section transmission electron microscopy by polishing and dimpling. Samples are thinned to electron transparency using a low-angle stage for the Fischione 1010 ion mill. STEM measurements are performed on a FEI *Titan 80-300* electron microscope operated at 200 kV and configured with a CEOS probe-side aberration corrector, which allowed us to achieve a resolution 0.78 Å at working parameters. Fig. 3 shows a high resolution Z-contrast image of the interface. This image is taken along the Si [110] zone axis. It shows a well-ordered epitaxial relationship between the Si substrate, STO and $TiO_2$. The most likely interface structure is shown by the overlay in Fig. 3. This interface structure is used as the starting model in the DFT calculations.

## III. Results and discussion

The band offset is the fundamental physical parameter that largely affects the functionality of a heterostructure, owing to its profound effect on the carrier confinement and electronic transport along and across the interface. However, oxide heterointerfaces are not as well-understood as those between metals and semiconductors. The band alignment at oxide heterointerfaces has attracted considerable attention in the context of the high-*k* dielectric gate stack in field effect transistors [43-47]. More recently, the band alignment between complex oxides has been of great interest following the discovery of novel interfacial electronic phases emerging at the epitaxial complex oxide heterointerfaces [48-51]. To describe and control the band alignment between two materials, the interfacial chemistry of a given heterointerface has to be well understood [44,45,52-54].

### 1. Charge transfer and dielectric screening at the interface

To understand the mechanism of the band offset formation at the anatase/STO interface, let us first consider the Schottky limit when two oxide slabs are far apart so that there is no interaction between them. We consider $TiO_2$-terminated STO (001) and tensile-strained (2.8%) anatase $TiO_2$ (001) slabs separately. The calculated planar-averaged electrostatic potential of these isolated slabs as a function of distance in the (001) direction is shown in Fig. 4. By macroscopically averaging the potentials, we identify the reference energy positions [55-57] in the bulk regions of STO (001) and $TiO_2$ with respect to

the vacuum level, which is set to be at 0 eV. The relative position of the valence band maximum (VBM) with respect to the reference energy is then determined in two separate bulk calculations. Assuming a common vacuum level, we find the valence band offset $\Delta E_v$ (= $E_{VBM}$(STO) – $E_{VBM}$($TiO_2$)) to be 0.94 eV. The offset changes to 0.89 eV if a relaxed anatase film ($a = b$ = 3.766 Å) is considered, meaning that in the Schottky limit, tensile strain plays only a minor role in determining the band offset. The relatively large valence band offset can be traced to the difference in oxygen coordination between the two oxides, since in both materials the top of the valence band is formed predominantly by the oxygen *p*-states. This point will be further discussed in section III.2.

When two oxide slabs are brought into contact, chemical bonds are created that result in charge redistribution in conjunction with a structural distortion at the interface. Our physical interface model between anatase $TiO_2$ and STO (001) is shown in Fig. 5 (a) and is based on the STEM image in Fig. 3. Note that half of O at the "STO surface" is bonded to Ti of anatase, leading to 3-fold coordinated O ($O_{3\text{-fold}}$, site A), while the other half of O remains 2-fold coordinated ($O_{2\text{-fold}}$, site B). Ti at the STO surface is also bonded to O of anatase at site C. We first check the evolution of the interface electronic structure as 4, 6, or 8 MLs $TiO_2$ films are "deposited" (one anatase unit cell has four $TiO_2$ monolayers). There is no significant change in the interface electronic structure for the different coverages, and furthermore, after 6 MLs deposition, the bulk electronic structure is recovered in the middle layer of the anatase region. In what follows, we focus on the heterostructure with 8 MLs of anatase deposited on STO (001) (see Fig. 1) unless otherwise noted.

The valence band offset of the heterostructure can be written as $\Delta E_H = \Delta E_S + \Delta V$, where $\Delta E_H$ is the band offset of the actual heterostructure, $\Delta E_S$ is the band offset in the Schottky limit, and $\Delta V$ is the electrostatic potential drop at the interface due to the heterojunction formation. The valence band offset is calculated using the macroscopic average of the electrostatic potential [55-57], as shown in Fig. 5 (b). We calculate the valence band offset to be 0.76 eV, thus $\Delta V$ is -0.2 eV. This process is often described as the creation of an interface dipole or double layer involving charge transfer and subsequent dielectric screening at the interface [44,45].

Based on the Schottky limit result, we expect electron transfer from the STO valence band into $TiO_2$. There are two channels for charge transfer: chemical bond induced transfer [58] and transfer into evanescent gap states [59]. In Fig. 6, we show the charge redistribution at the interface, which is defined as

$$\delta\rho(x,y,z) = \rho(\text{heterostructure}) - \rho(\text{STO substrate}) - \rho(TiO_2 \text{ film}), \quad (4)$$

where $\rho$ is the valence charge density of a given structure. In Fig. 6 (a), we use the charge densities of the relaxed free-standing STO and $TiO_2$ slabs for $\rho$(STO substrate) and $\rho$($TiO_2$ film), respectively, while for the plots in Fig. 6 (b) we use those of the STO and $TiO_2$ slabs where ionic positions are kept as those in the heterostructure. The two dimensional (2D) and one dimensional (1D) projections are defined as:

$$\delta\rho(y,z) = \int_0^a \delta\rho(x,y,z)dx \text{ and } \delta\rho(z) = \int_0^a\int_0^a \delta\rho(x,y,z)dxdy \quad (5)$$

respectively, where *a* is the STO lattice parameter. First we note that the charge transfer is better represented in Fig. 6 (a) than (b). Then we observe that indeed, chemical bonds drive the charge transfer between O and Ti. Assuming that the chemical bonds locally modify the charge density, the density underneath the STO surface is shifted upward (towards anatase) and localized along the chemical bonds between O and Ti as shown in Fig. 6 (a). The charge transfer to evanescent states of $TiO_2$ decays rapidly within 2 MLs of anatase as seen in Fig. 8 (a), where the finite density of states in the gap (between zero and -1 eV), can be only seen in the first two MLs of anatase.

For oxide interfaces, Sharia *et al.* have pointed out the importance of screening by O lattice polarization [44]. They have shown that as the coordination number of interfacial O increases, the Born effective charge of O increases as well and, as a result, the band offset is pushed back to the Schottky limit owing to the enhanced screening ability of interfacial O. The same argument applies to the $TiO_2/SrTiO_3$ structure. We note that the $O_{2\text{-fold}}$ ions at the interface shift by 0.22 Å from the Ti plane toward the STO bulk side as shown in Fig. 5 (a). In Fig. 7, we show the calculated band offset as a function of position of the $O_{2\text{-fold}}$ ions in the (001) direction. Pushing the $O_{2\text{-fold}}$ ions back to the level of the Ti plane decreases the band offset from 0.76 eV to 0.06 eV. It suggests that lattice polarization by the $O_{2\text{-fold}}$ ions is indeed the main screening mechanism at the interface [44]. The potential change at the interface due to lattice polarization is given by [60,61]:

$$\Delta V(O_{2-fold}) = \frac{1}{a^2}\frac{Z^{*}{}_{O_{2-fold}}{}^{(T)}}{\varepsilon_0\varepsilon_\infty}\Delta u(O_{2-fold}), \qquad (6)$$

where *a* is the in-plane lattice parameter, $Z^{*}{}_{O_{2-fold}}{}^{(T)}$ is the Born effective charge of $O_{2\text{-fold}}$ along the (001) direction, $\Delta u(O_{2\text{-fold}})$ is the displacement of $O_{2\text{-fold}}$ with respect to the Ti plane in the (001) direction, and $\varepsilon_\infty$ is the optical dielectric constant. Assuming $\varepsilon_\infty \approx 6.2$ [62-64], we estimate the Z* of $O_{2\text{-fold}}$ at the interface to be -1.66. This number is consistent with the model developed in Ref. [44].

To gain further insight, we analyze the spatial evolution of the electronic structure of the anatase layer from the interface with STO to the surface. We plot the layer-by-layer projected density of states (pDOS) for the valence band in Fig. 8 (a). Noting that the middle layers of the $TiO_2$ film recover the bulk electronic structure, we find a valence band offset of 0.7 eV, consistent with that obtained by the average potential method. We plot the pDOS corresponding to Ti *d* orbitals and O *p* orbitals of a $TiO_2$ layer in the STO bulk region, the interfacial $TiO_2$ layer, and a $TiO_2$ layer in the bulk region of anatase in Fig. 8 (b). By comparing the pDOS of $O_{2\text{-fold}}$ and $O_{3\text{-fold}}$ at the interface and those in the STO and anatase bulk regions, we see that the change in the bonding configuration at the interface drives the downward shift of the valence band. We will further discuss the evolution of the local electronic structure induced by the change in the bonding configuration in section III.2 using the experimental EELS O *K* edge spectra across the interface.

To check the accuracy of the valence band offset computed within the LDA, we calculate quasi-particle (QP) corrections to the LDA eigenvalues using the *GW* method for bulk STO and $TiO_2$. The results are summarized in Table 1. The band offset within the *GW* formalism is calculated as:

$$\Delta E_{v-GW} = \Delta E_{v-LDA} - (\delta_{STO} - \delta_{TiO_2}), \qquad (7)$$

where $\Delta E_{v\text{-}LDA}$ is the valence band offset computed within DFT-LDA and $\delta_{STO}$ and $\delta_{TiO2}$ are the QP corrections to the LDA valence band maxima of $SrTiO_3$ and $TiO_2$, respectively. The conduction band offset can be corrected in a similar manner. Since for computing band offsets we are only interested in the valence band maxima and the conduction band minima, we only report the QP corrections at the R and Γ *k*-points for $SrTiO_3$, and at the Γ and X points for anatase. Using the values of $\delta_{STO}$ and $\delta_{TiO2}$ at these *k*-points from Table 1 in equation (7), we find a *GW* correction of only 0.04 eV to the valence band offset calculated within LDA. Hence, although there is a significant QP correction to the band gaps of the individual bulk compounds, the valence band offset within the DFT-LDA is reliable as most of the correction comes from the conduction band for both the compounds.

**2. EELS O *K* edge spectra across the interface**

Experimentally, the evolution of the electronic structure across the interface can be monitored using EELS [65]. We perform a similar measurement with atomic resolution across the region indicated in Fig. 3. We focus on the O *K* edge spectra [66-68] rather than Ti $L_{2,3}$ edge spectra [69-71], as the O *K* edge in STO and $TiO_2$ better reflects the change in the local bonding environment (see Fig. 9 (a)) [65,72]. Theoretically, to include the effect of core holes generated in experiment, we employ the so-called *Z*+1 approximation [73,74] in our calculations. We replace the O atom under investigation with fluorine and calculate the 2*p*-projected DOS of the conduction band at that site [72]. In this way, one can create a positive charge in the core region and take into account the screening effect of the valence electrons. Using separate bulk calculations, we have first confirmed that increasing the in-plane cell size from 1×1 to $\sqrt{2}\times\sqrt{2}$ is sufficient to separate the core hole from its periodic images. We also find that the core hole effect is small for the O *K* edge spectra; and we only use it to make a few important spectral features more pronounced. In Fig. 9 (b), we plot the experimental EELS spectra along with the corresponding theoretical pDOS. Both are broadened using the Gaussian convolution method with a full width at half maximum value of 0.7 eV.

At the bottom of Fig. 9 (b), we compare the O *K* edge spectrum taken from the STO bulk region to the 2*p* pDOS calculated at the O site in the STO bulk region of the supercell. In experiment, we observe three main features between 530 eV and 550 eV, which are well reproduced in theory. Analyzing the entire set of pDOS's including contributions from the nearest neighbor Ti and Sr, we identify that the first, second, and third main peaks are derived from the interaction with Ti $t_{2g}$, Sr *d*, and Ti 4*sp* states, respectively. The Ti $e_g$ peak is seen as a small peak in theory between the first $t_{2g}$ and the second Sr *d* main peaks. However, as the $e_g$ band is largely broadened in STO with a bandwidth of about 5 eV, the $e_g$ peak is not seen experimentally owing to the presence of the adjacent large Sr *d* peak.

Looking at the spectrum taken from the anatase bulk region (see Fig. 9 (b)), we observe quite different spectral features. First, the $e_g$ and $t_{2g}$ peaks become sharp and pronounced at position A compared to that of STO. Secondly, the Sr *d* peak is absent at position B, as there is no Sr on the $TiO_2$ side of the interface. Thirdly and most importantly, there is the appearance of a large spectral weight between 538 eV and 543 eV (position C), which is not found on the STO side. This peak turns out to be derived from the

interaction with the nearest neighbor O along the *c*-axis. In Fig. 9 (a) we show a schematic of the $TiO_2$ plane in STO and anatase. Although the basic building block in both materials is a $TiO_6$ octahedron, the connecting geometry is different: the octahedra share corners in STO while they share four adjacent edges in anatase. In contrast to the straight Ti-O chain along the *a* or *b* axes in STO, it exhibits a zigzag pattern in anatase as shown in Fig. 9 (a). In other words, for a given octahedron in anatase, two O atoms in the *ab*-plane are shifted upward along the *c*-direction and the other two are shifted down with respect to the central Ti atom. This crystallographic feature leads to appreciable π-type overlap between O 2*p* orbitals along the *c*-direction as shown in Fig. 9 (a). Finally, we remark that this spectral peak originally emerges at the interface as shown in the middle of Fig. 9 (b). By comparing with the 2*p* pDOS at the $O_{3\text{-fold}}$ site of the interfacial layer (site A in Fig. 5 (a)), we infer that this peak at the interface reflects the chemical bond formation between anatase and STO.

**3. Oxygen vacancy and fluorine impurity at the $TiO_2/SrTiO_3$ interface**

DFT calculations reported in [31] suggested a valence band offset of 0.5 eV, consistent with our results but in apparent variance with the measurement. To better understand this discrepancy, we consider two types of interface defects, an oxygen vacancy and a substitutional fluorine impurity. For these calculations, we increase the in-plane cell size from 1×1 to $\sqrt{2}\times\sqrt{2}$ to allow for more structural degrees of freedom at the interface. We consider a 6 ML thick $TiO_2$ overlayer on STO (001).

In previous sections, we have established that interfacial O plays a crucial role in determining the dielectric response of the heterointerface. This brings a natural question: what would be the effect on the band alignment of an interfacial O vacancy? [75] Here we only consider a neutral vacancy. There are four types of interfacial O ions as shown in Fig. 5 (a). We find that a vacancy at site B is the most stable configuration. The O vacancy formation energy at this site is calculated to be 3.8 eV while those of the A, C and D sites are 1.6, 1.1, and 1.4 eV higher in energy, respectively. The formation energy of 3.8 eV is significantly lower than, for example, that of a neutral O vacancy in bulk STO, which is larger than 6.0 eV [76]. In section III.1, we have shown that O at site B is responsible for the screening of the interfacial dipole. Therefore, one can expect that the band offset would be significantly reduced by a vacancy at this site, as the charge transfer that tends to equilibrate the Fermi level of two oxides will not be fully screened. Using the average potential method, we calculate the band offset for the interface with a vacancy to be 0.04 eV as shown in Fig. 10 (a). The absence of the valence band offset in the presence of a vacancy is also seen in the pDOS of the heterostructure in Fig. 10 (b).

In addition, we consider a substitutional F impurity at the STO surface, which could be present when the STO substrate is etched in buffered HF solution in order to have a 1×1 $TiO_2$-terminated surface [31]. It has been suggested in Ref. [31] that F substitutes O at the STO surface and the mole fraction within the XPS probe depth (~45Å) has been estimated to be about 5%. We consider all four interfacial O sites A, B, C, and D for the F substitution. We find that the most stable structure is obtained when F is substituted for 2-fold O at the B site. The relaxed structure for this configuration is shown in Fig. 11 (a). F at the A, C, and D sites is higher in energy by 1.1, 0.7, and 0.8 eV, respectively. As mentioned earlier, 2-fold O at the B site is responsible for screening the interface dipole. Since F has lesser formal ionic charge of -1*e* versus -2*e* of O, one would expect that the effective charge of F at the interface is also reduced by about a factor of two. Furthermore, as shown in Fig. 11 (a), substituted F does not polarize, while the rest of 2-

fold O on the STO surface polarize toward the STO side by 0.27 Å. We attribute this to a much shorter Ti-F bond length (1.75 Å in $TiF_4$ is [77]), as compared to the Ti-O bond length of 1.95 Å in STO. Therefore, we expect that the dielectric screening at the interface is significantly reduced by the F substitution. We plot the layer by layer pDOS in Fig. 11 (b), showing a negligible valence band offset of less than 0.1 eV between STO and $TiO_2$ in the presence of F at the interface. The average potential method gives a comparable offset of 0.3 eV, which is consistent with the pDOS offset.

Thus, we argue that interfacial impurities such as an O vacancy or substitutional fluorine may be responsible for the experimentally observed absence of a valence band offset at the anatase $TiO_2$/STO interface [31]. It is worth noting, that other mechanisms such as cationic exchange may also contribute to the disappearance of the valence band offset. For example, Ciancio *et al.* have observed a Sr-deficient epitaxial interphase at the $TiO_2$/STO interface grown by pulsed laser deposition (PLD) [78,79]. This interphase formation has been attributed to the long range migration of Sr from the STO substrate to the anatase film.

## V. Conclusions

In summary, we studied the interfacial atomic structure and electronic structure of anatase $TiO_2$/STO (001) heterostructure grown on Si by molecular beam epitaxy using density function theory and scanning transmission electron microscopy. Theoretically, the interface is described at the local density approximation level. By analyzing the layer-by-layer pDOS and EELS O *K* edge spectra we show that the evolution of the valence band across the interface is driven by the change in bonding configuration. The main results are summarized as follows: (i) in the Schottky limit, the STO valence band top (VBT) is higher in energy by 0.94 eV than that of $TiO_2$; (ii) charge transfer from STO to $TiO_2$ occurs mainly through the chemical bonds at the interface and equilibrates the Fermi level by forming a double layer. However, subsequent polarization of the $O_{2\text{-fold}}$ lattice largely screens the interfacial dipole, yielding a net valence band offset of 0.76 eV; (iii) the quasi-particle correction obtained with the *GW* method is large for the conduction band edge while the valence band edges of STO and $TiO_2$ are not altered. This supports the validity of the LDA result for the occupied valence band line-up; (iv) comparing the EELS O *K* edge spectra and the 2*p*-symmetry projected density of states across the interface, we show that the transition from $O_h$ symmetry for $TiO_6$ with 2-fold coordinated O in STO to the tetragonal $D_{2d}$ symmetry with 3-fold O in anatase drives the evolution of the valence band. One of the main features is the appearance of a $\pi$-type oxygen-oxygen interaction along the *c*-direction. In addition, considering an interfacial O vacancy and F impurity, we show that the most stable vacancy or impurity site is the $O_{2\text{-fold}}$ site that is responsible for the screening of the dipole layer. As a result, the band offset is significantly reduced in the presence of O vacancy or F impurity at the interface suggesting that the perceived absence of a valence band offset [31] is not intrinsic.

## Acknowledgements

This work is supported by the National Science Foundation under Grant No. DMR-0548182, US Department of Energy (DOE) under Grant No. DE-SC0001878, Office of Naval Research under Grant N000 14-10-1-0489, and Texas Advanced Computing Center.

**References**


[1] B. O'Regan and M. Grätzel, Nature **353**, 737 (1991).
[2] A. Fujishima, X. Zhang, and D. A. Tryk, Surf. Sci. Rep. **63,** 515 (2008).
[3] X. Chen, S. Shen, L. Guo, and S. S. Mao, Chem. Rev. **110**, 6503 (2010).
[4] N. S. Lewis and D. G. Nocera, Proc. Natl. Acad. Sci. **103**, 15729 (2006).
[5] A. L. Linsebigler, G. Lu, and J. T. Yates, Chem. Rev. **95**, 735 (1995).
[6] H. G. Yang, C. H. Sun, S. Z. Qiao, J. Zou, G. Liu, S. C. Smith, H. M. Cheng, G. Q. Lu, Nature **453**, 638 (2008).
[7] A. Selloni, Nat. Mater. **7**, 613 (2008).
[8] L. Forro, O. Chauvet, D. Emin, L. Zuppiroli, H. Berger, and F. Lévy, J. Appl. Phys. **75**, 633 (1994).
[9] H. Tang, K. Prasad, R. Sanjinès, and F. Lévy, J. Appl. Phys. **75**, 2042 (1994).
[10] M. Xu, Y. Gao, E. M. Moreno, M. Kunst, M. Muhler, Y. Wang, H. Idriss, and C. Wöll, Phys. Rev. Lett. **106**, 138302 (2011).
[11] F. E. Osterloh and B. A. Parkinson, MRS Bulletin **36**, 17 (2011).
[12] R. Asahi, T. Morikawa, T. Ohwaki, K. Aoki, and Y. Taga, Science **293**, 269 (2001).
[13] Y. Gai, J. Li, S. Li, J. Xia, and S. Wei, Phys. Rev. Lett. **102**, 036402 (2009).
[14] W. Zhu, X. Qiu, V. Iancu, X. Chen, H. Pan, W. Wang, N. M. Dimitrijevic, T. Rajh, H. M. Meyer III, M. Parans Paranthaman, G. M. Stocks, H. H. Weitering, B. Gu, G. Eres, and Z. Zhang, Phys. Rev. Lett. **103**, 226401 (2009).
[15] X. Chen, L. Liu, P. Y. Yu, S. S. Mao, Science **331**, 746 (2011).
[16] T. Ohno, K. Sarukawa, K. Tokieda, and M. Matsumura, J. of Catal. **203**, 82 (2001).
[17] D. C. Hurum, A. G. Agrios, and K. A. Gray, J. Phys. Chem. B **107**, 4545 (2003).
[18] N. Siedl, M. J. Elser, J. Bernardi, and O. Diwald, J. Phys. Chem. C **113**, 15792 (2009).
[19] D. L. Liao, C. A. Badour, and B. Q. Liao, J. Photochem. and Photobiol. A **194**, 11 (2008).
[20] N. Nilius, T. Risse, S. Schauermann, S. Shaikhutdinov, M. Sterrer, H. –J. Freund, Top. Catal. **54**, 4 (2011).
[21] S. A. Chambers, C. M. Wang, S. Thevuthasan, T. Droubay, D. E. McCready, A. S. Lea, V. Shutthanandan and C. F. Wndisch Jr, Thin Solid Films **418**,197 (2002).
[22] Z. Wang, W. Zeng, L. Gu, M. Saito, S. Tsukimoto, and Y. Ikuhara, J. Appl. Phys. **108**, 113701 (2010).
[23] N. V. Burbure, P. A. Salvador, and G. S. Rohrer, Chem. Mater. **22**, 5823 (2010).
[24] D. Kazazis, S. Guha, N. A. Bojarczuk, A. Zaslavsky, and H. –C. Kim, Appl. Phys. Lett. **95**, 064103 (2009).
[25] R. Shao, C. Wang, D. E. McCready, T. C. Droubay, S. A. Chambers, Surf. Sci. **601**, 1582 (2007).
[26] H. Ohta, S. Kim, Y. Mune, T. Mizoguchi, K. Nomura, S. Ohta, T. Nomura, Y. Nakanishi, Y. Ikuhara, M. Hirano, H. Hosono, and K. Koumoto, Nat. Mater. **6**, 129 (2007).
[27] Y. Matsumoto, M. Murakami, T. Shono, T. Hasegawa, T. Fukumura, M. Kawasaki, P. Ahmet, T. Chikyow, S. Koshihara, H. Koinuma, Science **291**, 854 (2001).
[28] M. Katayama, S. Ikesaka, J. Kuwano, H. Koinuma, and Y. Matsumoto, Appl. Phys. Lett. **92**, 132107 (2008).
[29] T. C. Kaspar, T. Droubay, V. Shutthanandan, S. M. Heald, C. M. Wang, D. E. McCready, S. Thevuthasan, J. D. Bryan, D. R. Gamelin, A. J. Kellock, M. F. Toney, X. Hong, C. H. Ahn, and S. A. Chambers, Phys. Rev. B. **73**, 155327 (2006).

[30] Y. Yamada, K. Ueno, T. Fukumura, H. T. Yuan, H. Shimotani, Y. Iwasa, L. Gu, S. Tsukimoto, Y. Ikuhara, M. Kawasaki, Science **332**, 1065 (2011).
[31] S. A. Chambers, T. Ohsawa, C. M. Wang, I. Lyubinetsky, J. E. Jaffe, Surf. Sci. **603,** 771 (2009).
[32] M. Choi, A. Posadas, R. Dargis, C. Shih, and A. A. Demkov, J. Appl. Phys. **111**, 064112 (2012).
[33] G. Kresse and J. Furthmüller, Phys. Rev. B. **54**, 11169 (1996).
[34] J. P. Perdew and A. Zunger, Phys. Rev. B **23**, 5048 (1981).
[35] P. E. Blöchl, Phys. Rev. B **50**, 17953 (1994).
[36] R. Loetzsch, A. Lübcke, I. Uschmann, E. Förster, V. Groβe, M. Thuerk, T. Koettig, F. Schmidl, and P. Seidel, Appl. Phys. Lett. **96**, 071901 (2010).
[37] D. R. Hummer, P. J. Heaney, and J. E. Post, Powder Diffraction **22**, 352 (2007).
[38] M. Shishkin and G. Kresse, Phys. Rev. B **74**, 035101 (2006).
[39] L. Hedin, Phys. Rev **139**, A796 (1965).
[40] M. S. Hybertsen and S. G. Louie, Phys. Rev. B **32**, 7005 (1985).
[41] W. Wei, X. Hu, Y. Liang, D. Jordan, B. Craigo, R. Droopad, Z. Yu, A. A. Demkov, J. Edward, Jr., and W. Ooms, J. Vac. Sci. Technol. B **20**, 1402 (2002).
[42] R. A. McKee, F. J. Walker, and M. F. Chisholm, Phys. Rev. Lett. **81**, 3014 (1998).
[43] A. A. Demkov, L. R. C. Fonseca, E. Verret, J. Tomfohr, and O. F. Sankey, Phys. Rev. B **71**, 195306 (2005).
[44] O. Sharia, A. A. Demkov, G. Bersuker, and B. H. Lee, Phys. Rev. B **75**, 035306 (2007).
[45] X. Luo, G. Bersuker, and A. A. Demkov, Phys. Rev. B **84**, 195309 (2011).
[46] J. Junquera, M. Zimmer, P. Ordejón, and P. Ghosez, Phys. Rev. B **67**, 155327 (2003).
[47] K. Kita and A. Toriumi, Appl. Phys. Lett. **94**, 132902 (2009).
[48] A. Ohtomo and H. Y. Hwang, Nature **427**, 423 (2004).
[49] J. K. Lee and A.A. Demkov, Phys. Rev. B **78**, 193104 (2008).
[50] J. K. Lee, N. Sai, and A. A. Demkov, Phys. Rev. B **82**, 235305 (2010).
[51] M. Nakamura, A. Sawa, J. Fujioka, M. Kawasaki, and Y. Tokura, Phys. Rev. B **82**, 201101(R) (2010).
[52] R. A. McKee, F. J. Walker, M. B. Nardelli, W. A. Shelton, and G. M. Stocks, Science **300**, 1726 (2003).
[53] Y. Hikita, M. Nishikawa, T. Yajima, and H. Y. Hwang, Phys. Rev. B **79**, 073101 (2009).
[54] J. D. Burton and E. Y. Tsymbal, Phys. Rev. B **82**, 161407 (2010).
[55] L. Kleinman, Phys. Rev. B **24**, 7412 (1981).
[56] D. M. Bylander and L. Kleinman, Phys. Rev. B **36**, 3229 (1987).
[57] C. G. Van de Walle, Phys. Rev. B **39**, 1871 (1989).
[58] R. T. Tung, Phys. Rev. Lett. **84**, 6078 (2000).
[59] J. Tersoff, Phys. Rev. B **32**, 6968 (1985).
[60] R. M. Martin and K. Kunc, Phys. Rev. B **24**, 2081 (1981).
[61] Ph. Ghosez, J. –P. Michenaud, and X. Gonze, Phys. Rev. B **58**, 6224 (1998).
[62] M. Mikami, S. Nakamura, O. Kitao, and H. Arakawa, Phys. Rev. B **66**, 155213 (2002).
[63] R. J. Gonzalez, R. Zallen, and H. Berger, Phys. Rev. B **55**, 7014 (1997).
[64] C. J. Fennie and K. M. Rabe, Phys. Rev. B **68**, 184111 (2003).
[65] D. A. Muller, Nat. Mater. **8**, 263 (2009).
[66] F. M. F. de Groot, J. Faber, J. J. M. Michiels, M. T. Czyżyk, M. Abbate, and J. C. Fuggle, Phys. Rev. B **48**, 2074 (1993).

[67] K. van Benthem, C. Elsässer, M. Rühle, Ultramic. **96**, 509 (2003).
[68] D. A. Muller, T. Sorsch, S. Moccio, F. H. Baumann, K. Evans-Lutterodt, and G. Timp, Nature **399**, 758 (1999).
[69] R. Laskowski and P. Blaha, Phys. Rev. B **82**, 205104 (2010).
[70] K. Ogasawara, T. Iwata, Y. Koyama, T. Ishii, I. Tanaka, and H. Adachi, Phys. Rev. B **64**, 115413 (2001).
[71] P. Krüger, Phys. Rev. B **81**, 125121 (2010).
[72] D. A. Muller, D. J. Singh, and J. Silcox, Phys. Rev. B **57**, 8181 (1998).
[73] C. Elsässer, S. Köstlmeier, Ultramic. **86**, 325 (2001).
[74] G. Duscher, R. Buczko, S. J. Pennycook, S. T. Pantelides, Ultramic. **86**, 355 (2001).
[75] X. Weng, P. Fisher, M. Skowronski, P. A. Salvador, and O. Maksimov, J. Cryst. Growth. **310**, 545 (2008).
[76] C. Mitra, C. Lin, J. Robertson, and A. A. Demkov, *to be published* (2012).
[77] K. D. Dobbs and W. J. Hehre, J. Comp. Chem. 8, 880 (1987).
[78] R. Ciancio, E. Carlino, C. Aruta, D. Maccariello, F. M. Granozio, and U. S. di Uccio, Nanoscale, **4**, 91 (2012).
[79] M. Radović, M. Salluzzo, Z. Ristić, R. di Capua, N. Lampis, R. Vaglio, and F. M. Granozio, J. Chem. Phys. **135**, 034705 (2011).

**Tables**

**Table I.** *GW* quasi-particle (QP) corrections for $SrTiO_3$ and anatase $TiO_2$.

| Material | CBM, δ* (*k*-point/eV) | VBM, δ* (*k*-point/eV) |
|---|---|---|
| $SrTiO_3$ | Γ/1.9, R/2.1 | Γ/-0.1, R/-0.06 |
| $TiO_2$ | Γ/1.97, X/1.93 | Γ/-0.15, X/-0.02 |

*δ's for the conduction band minimum (CBM) and the valence band maximum (VBM) are defined by $E^{LDA}$-$E^{QP}$ at the CBM and VBM, respectively.

**Figure captions**

FIG. 1. (Color online) Slab model of the 8ML anatase $TiO_2/SrTiO_3$ (001) heterostructure.

FIG. 2. RHEED patterns for (a) an STO film on Si (001) taken along the Si<110> direction; and (b) for a 20 monolayer anatase film taken along the same direction (b).

FIG. 3. (Color online) Z-contrast HRTEM image of the $TiO_2/SrTiO_3$/Si (001) structure. Blue (Ti) and green (Sr) balls are superimposed at the $TiO_2/SrTiO_3$ interface as a guide to the eye. Spatially resolved EELS measurement is performed at the region indicated by the orange box.

FIG. 4. (Color online) Planar-averaged electrostatic potentials along the (001) direction for free-standing STO (left) and $TiO_2$ slabs (right). Macroscopically averaged potential profiles are shown in blue. Energy position of valence band maximum (VBM) in the bulk region of each slab with respect to the reference potential energy is indicated with the green line. Dotted green lines are drawn for comparison of the two VBM positions to visualize the Schottky-limit band offset.

FIG. 5. (Color online) (a) Interface model between anatase $TiO_2$ and STO (001). Black arrows show the relaxation pattern of the O ions at the interface. (b) Planar-averaged electrostatic potential of the heterostructure along the (001) direction. The straight black lines indicate the reference electrostatic energy positions with respect to the vacuum level (0 eV) in the bulk region of STO and $TiO_2$, respectively. The green lines indicate the relative positions of VBM of STO and $TiO_2$ with respect to their corresponding reference energy positions.

FIG. 6. (Color online) Two-dimensional (left) and one-dimensional (right) projections of the charge redistribution ($\delta\rho(x,y,z)$) at the $TiO_2/SrTiO_3$ (001) interface (see text). For the reference charge density of the free-standing STO and $TiO_2$ slabs, we use relaxed (a) or un-relaxed (b) atomic geometry.

FIG. 7. (Color online) Band offset and total energy of the $TiO_2$/STO heterostructure as a function of the displacement of $O_{2\text{-fold}}$ ions at the interface. The inset is a schematic picture to show the lattice polarization by $O_{2\text{-fold}}$ at the interface. In the relaxed heterostructure, the optimal $\Delta z$ is -0.22 Å, where the energy is minimum.

FIG. 8. (Color online) (a) Layer-by-layer projected density of states (pDOS) of the $TiO_2/SrTiO_3$ (001) heterostructure. The green line is the Fermi level. (b) Atom-resolved pDOS of the $TiO_2$ layer at the STO bulk (bottom), interface (middle), and $TiO_2$ bulk (top) regions.

FIG. 9. (Color online) (a) Schematic pictures of a $TiO_2$ plane in bulk STO (left) and bulk anatase $TiO_2$ (right) (b) EELS O *K* edge spectra taken at the interface from the STO side (two bottom spectra) to the anatase $TiO_2$ side (two upper spectra) through the interface (two middle green spectra). The corresponding 2*p*-projected DOS's are overlaid in grey.

FIG. 10. (Color online) (a) Planar-averaged electrostatic potential of the heterostructure in the presence of an interfacial O vacancy. The straight black lines indicate the reference electrostatic energy positions with respect to the vacuum level. The green lines show the relative positions of VBM of $SrTiO_3$ and $TiO_2$ with respect to their reference energy positions. (b) Layer-by-layer valence band pDOS of the heterostructure in the presence of an interfacial O vacancy. The dotted straight line is placed at the VBM in the STO bulk region and is extended into the $TiO_2$ side for comparison.

FIG. 11. (Color online) . (a) Relaxed atomic structure of the $TiO_2/SrTiO_3$ (001) interface in the presence of an interfacial F impurity. (b) Layer-by-layer valence band pDOS of the heterostructure in the presence of the interfacial F impurity. The dotted line is placed at the VBM in the STO bulk region and extended across into the $TiO_2$ side for comparison.

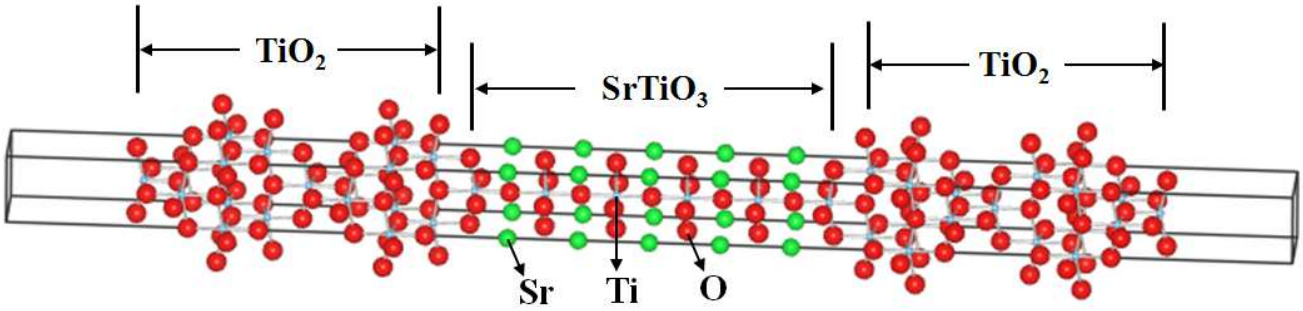


Figure 1 BS12022 18JUL2012

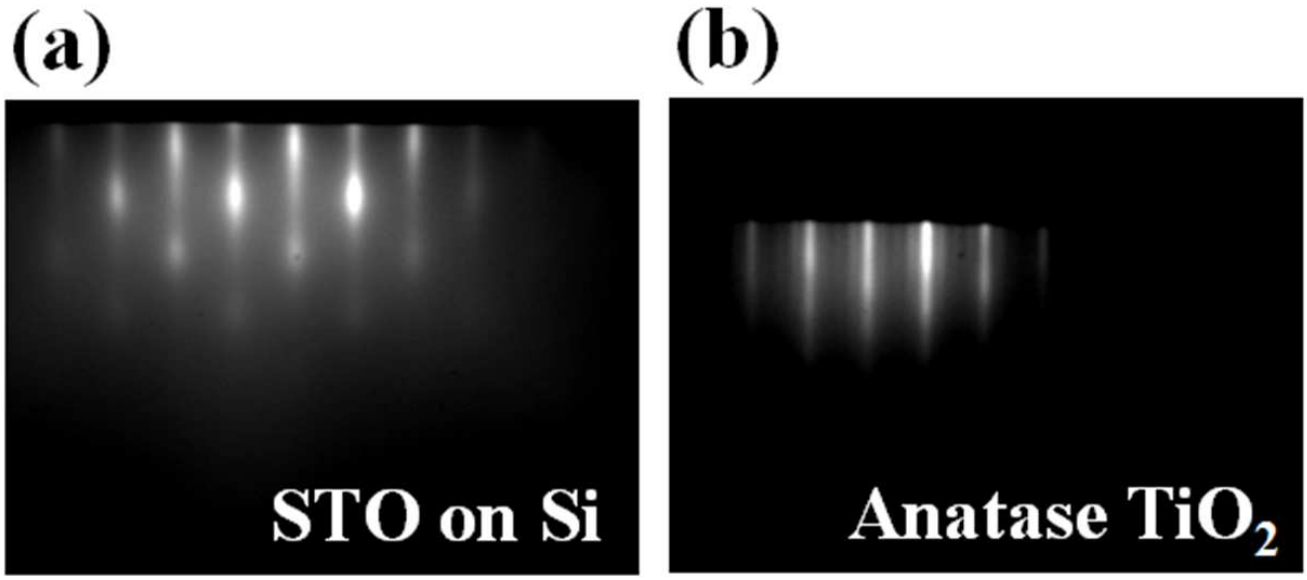


Figure 2 BS12022 18JUL2012

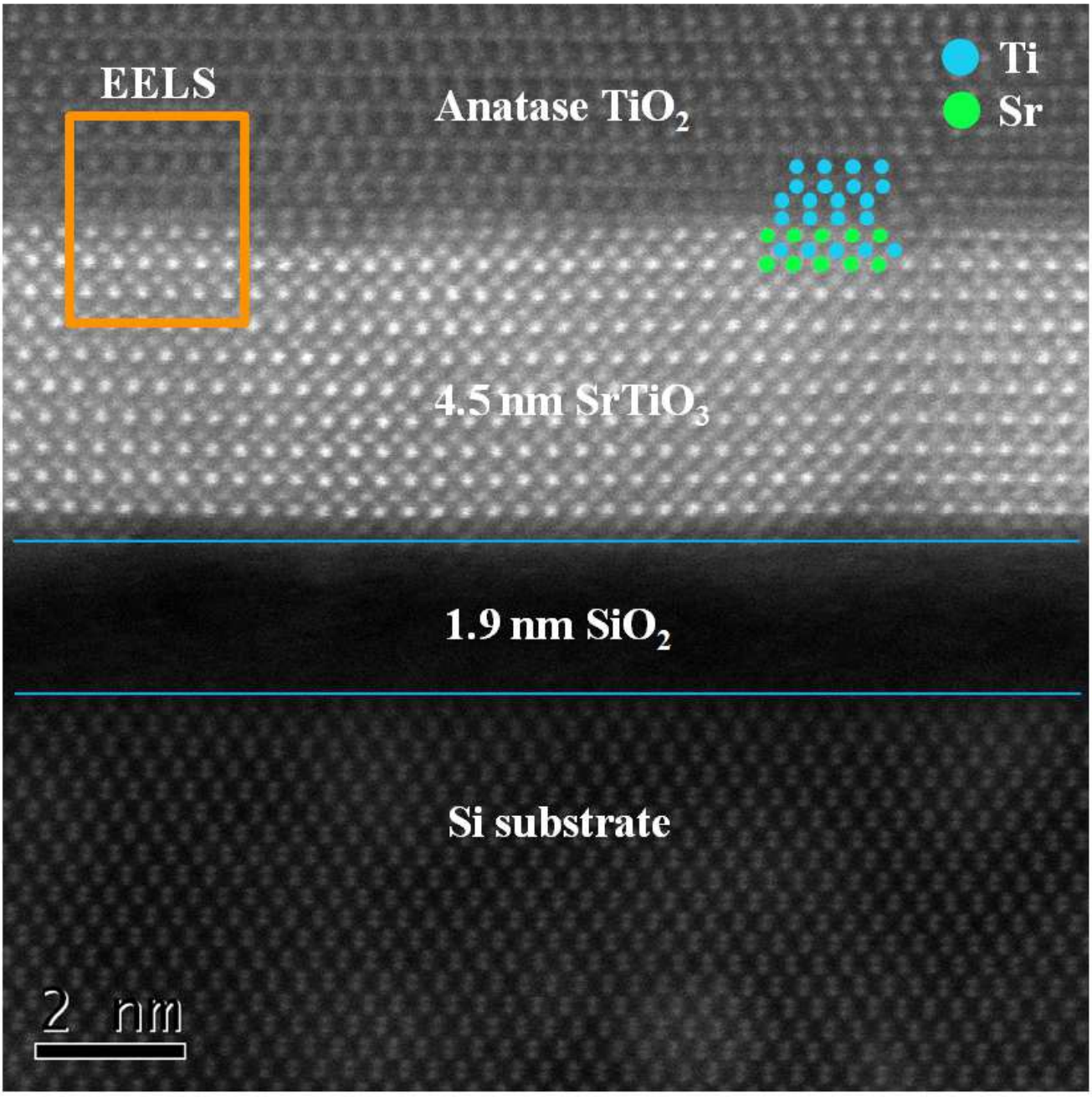


Figure 3 BS12022 18JUL2012

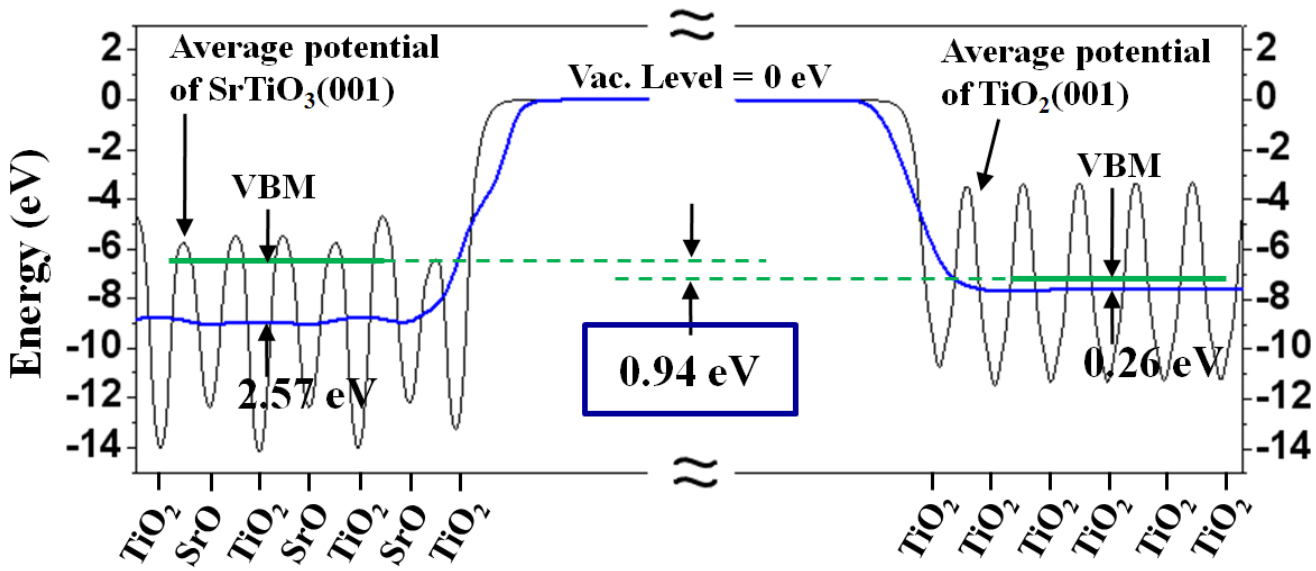


Figure 4 BS12022 18JUL2012

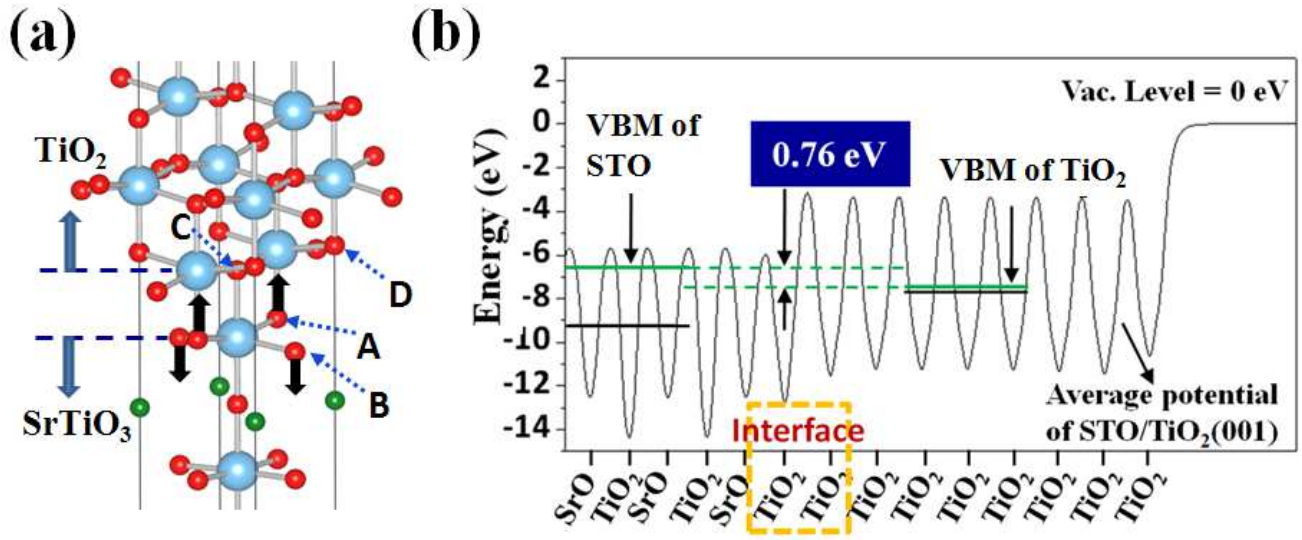


Figure 5 BS12022 18JUL2012

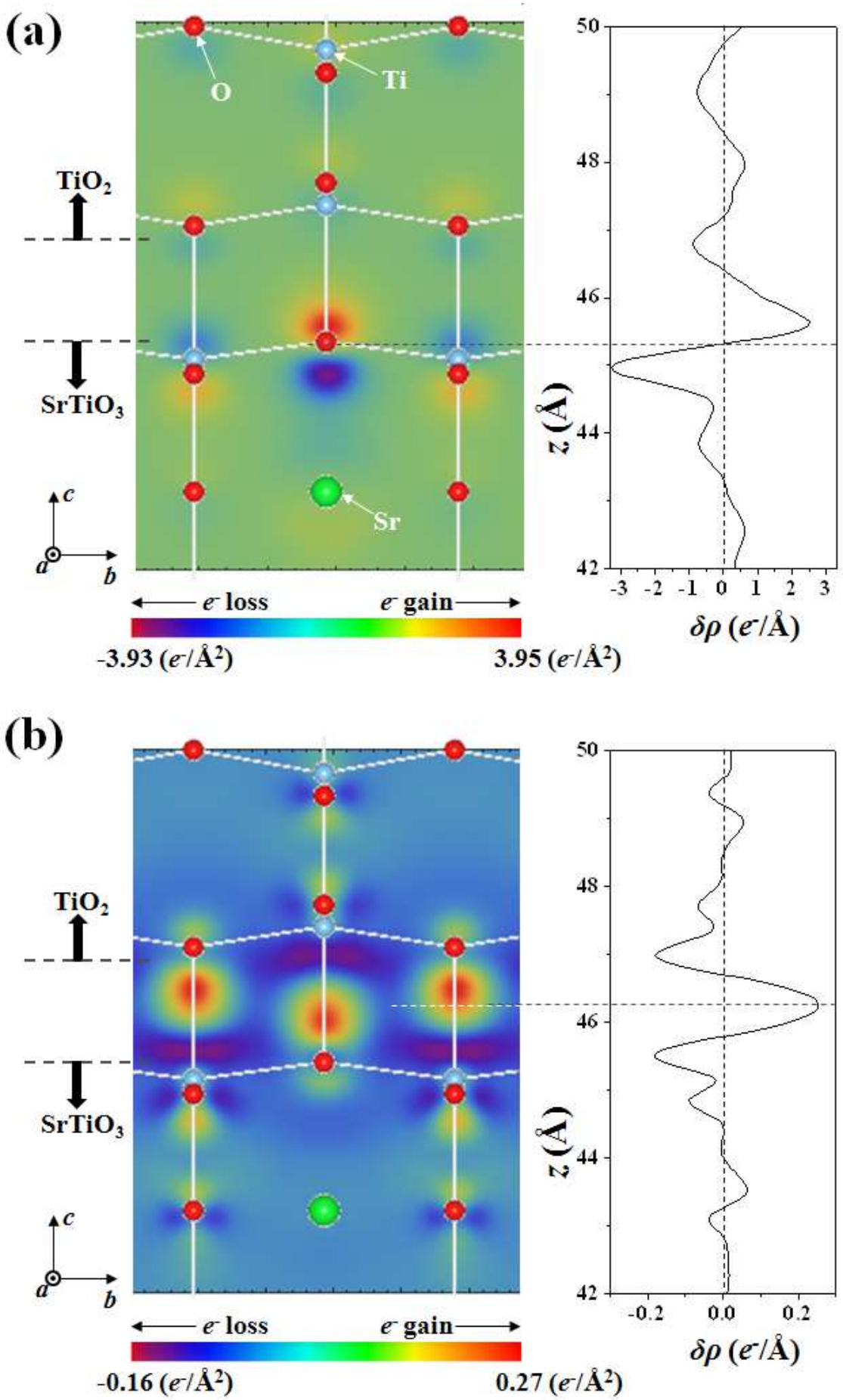


Figure 6 BS12022 18JUL2012

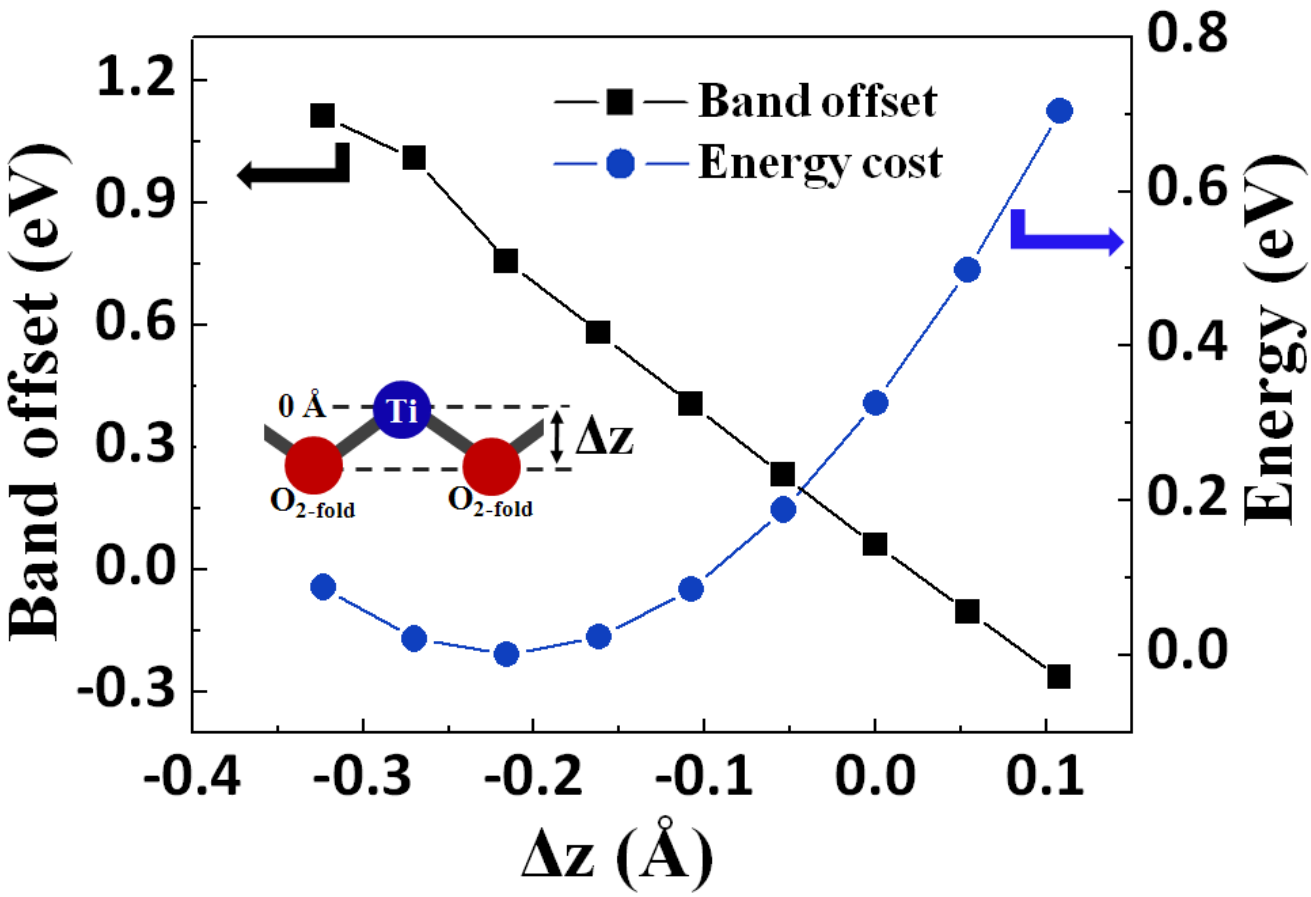


Figure 7 BS12022 18JUL2012

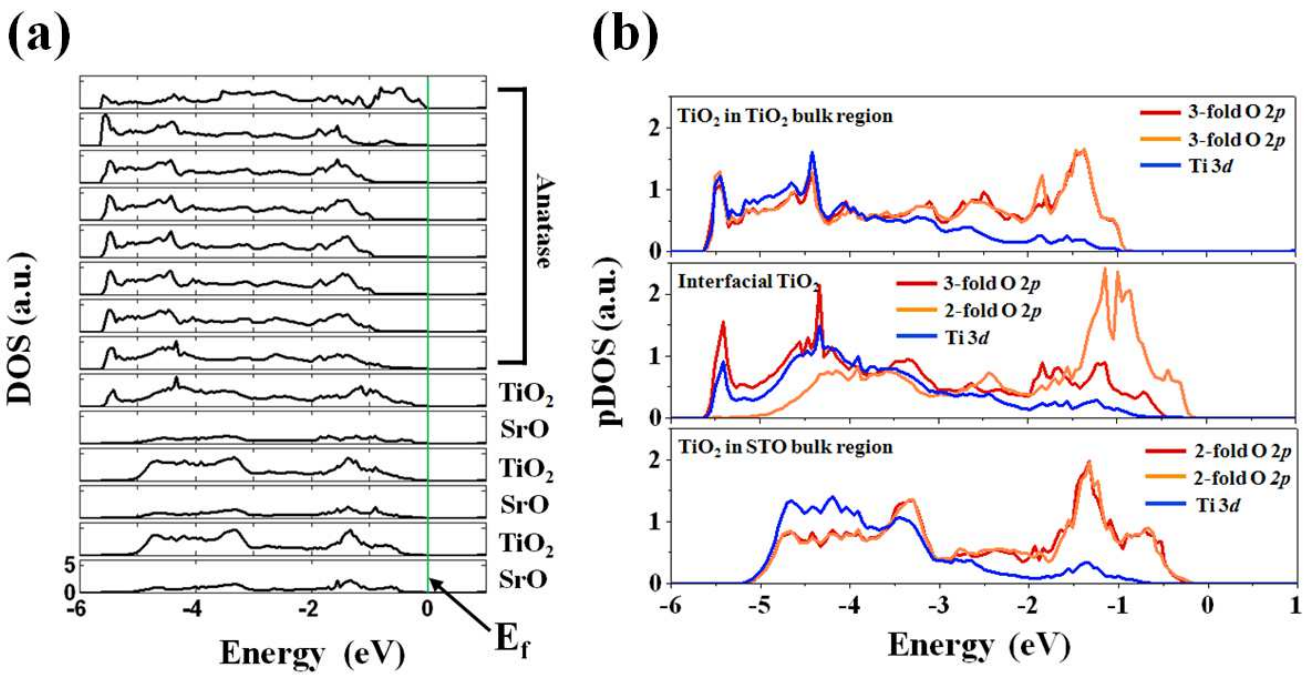


Figure 8 BS12022 18JUL2012

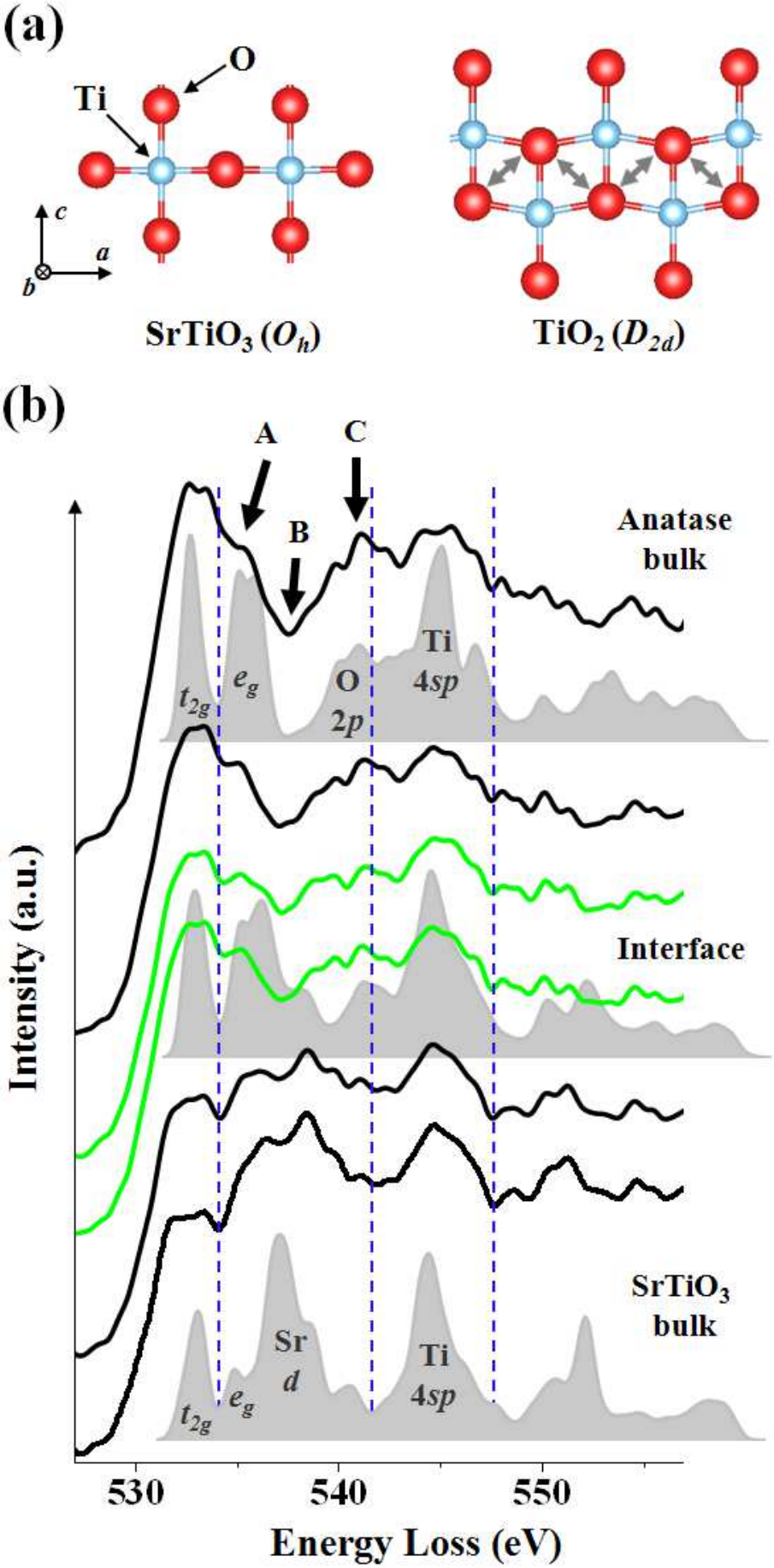


Figure 9 BS12022 18JUL2012

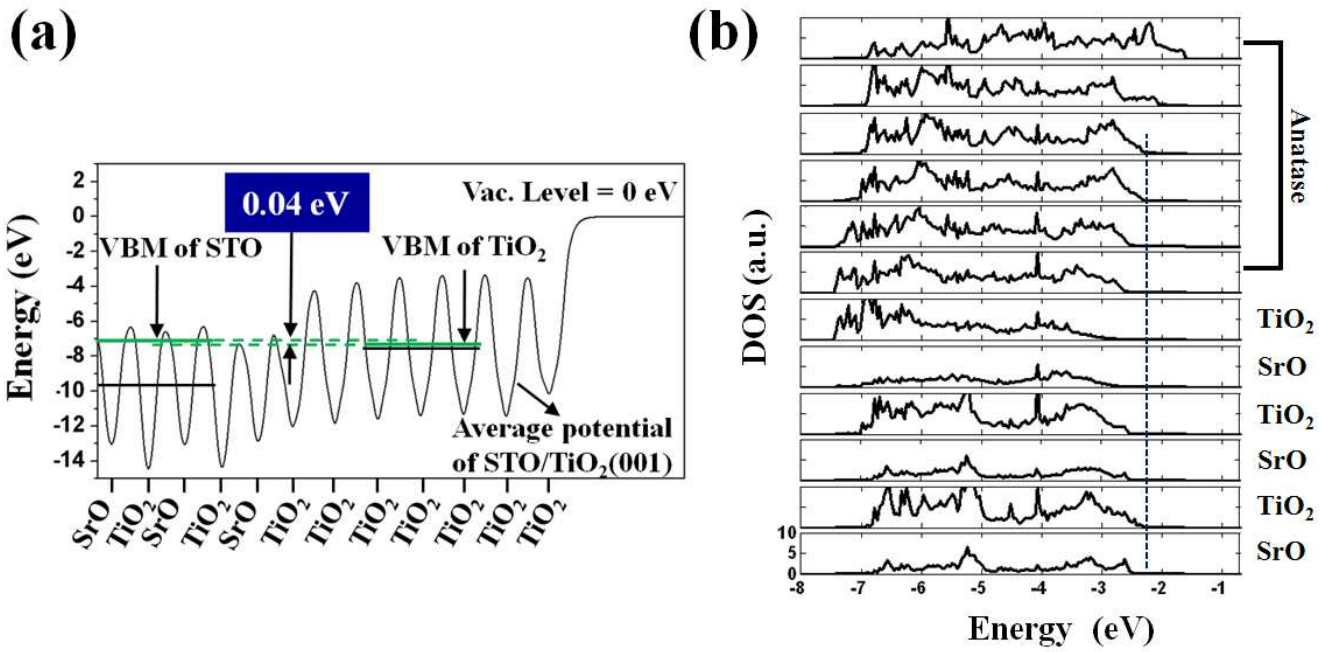


Figure 10 BS12022 18JUL2012

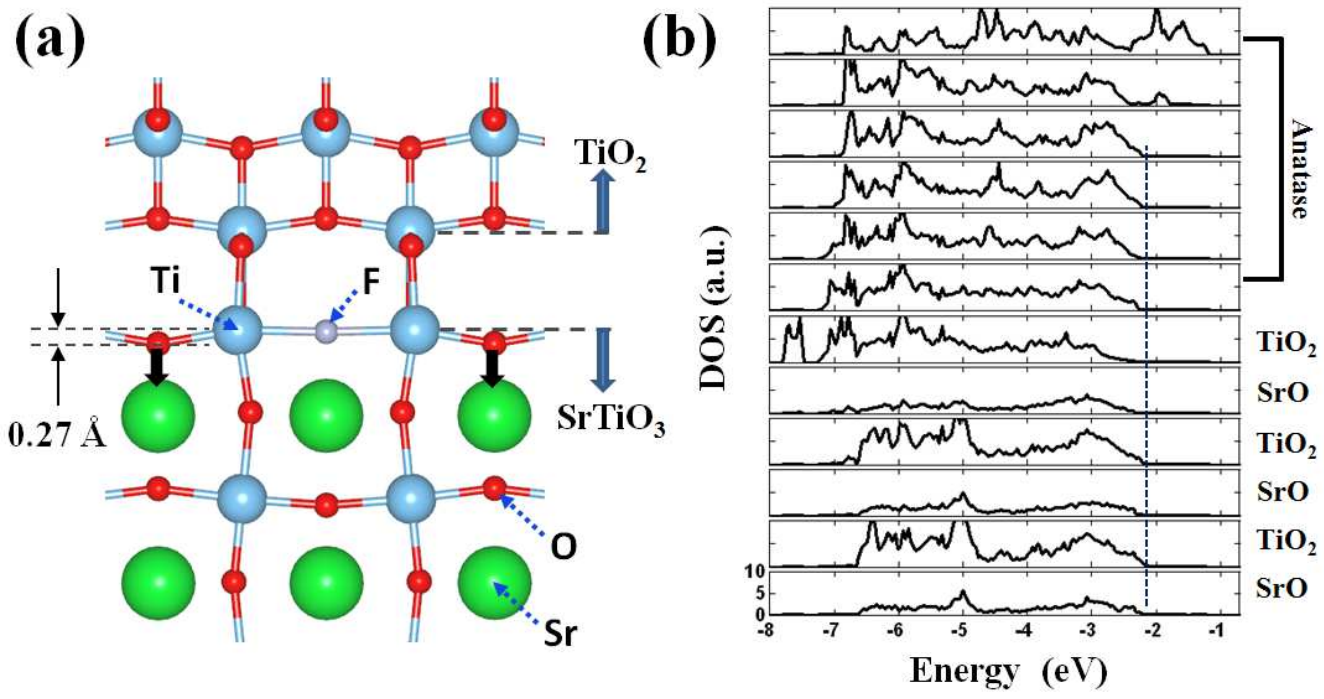


Figure 11 BS12022 18JUL2012